JOURNAL OF AIRCRAFT
Vol. 39, No. 5, September–October 2002

Rotary-Wing Wake Capturing: High-Order Schemes Toward Minimizing Numerical Vortex Dissipation

Nathan Hariharan*
United Technologies Research Center, East Hartford, Connecticut 06018

The use of high-order, first-principles-based Euler/Navier–Stokes methodologies for rotary-wing wake capturing is addressed. Fifth/seventh-order spatially accurate essentially nonoscillatory methodologies were implemented and their benefits in capturing wake vortices were assessed. The use of high-order solution reconstruction, in conjunction with the use of overset grids to resolve selectively regions of interest such as concentrated vorticity, was also explored. The tip vortex off of a NACA0015 wing was captured using this methodology, and the tip vortex characteristics are compared with experiments. The relative merits of fifth- and seventh-order schemes are assessed for capturing wake vorticity.

Nomenclature

$|A|$ = Roe's dissipation matrix
$\boldsymbol{F}$ = flux vector for inviscid fluxes
$\boldsymbol{F}_v$ = flux vector for viscous fluxes
$\boldsymbol{q}$ = vector of primitive flow variables
$\boldsymbol{q}_L$ = left-hand side flow vector at a given face
$\boldsymbol{q}_R$ = right-hand side flow vector at a given face
$\boldsymbol{V}_F$ = fluid velocity
$\boldsymbol{V}_G$ = grid velocity
ΔS = face surface area
Ω_J = cell volume

I. Introduction

ONE of the chief focuses of advanced helicopter designs for the next generation is the design of highly maneuverable, agile helicopters with excellent handling qualities. Such high-performance rotorcrafts are very desirable in air-to-air combat, deep penetration strikes, and ground support in hostile terrain. These abilities will enhance the capabilities of rescue missions involving rotorcraft operating at the edge of the design envelope. The other issue that needs to be tackled for the healthy growth of the helicopter industry in the civilian market is a more detailed understanding of noise generation and its control. The achievement of significant advances in the capabilities of rotorcraft will have to take advantage of advances in the area of aerodynamics, especially in the design of advanced rotor tip shapes that take into account the interplay between the rotor and the highly "vorticity-charged" flowfield surrounding it.

An important unresolved issue in the aerodynamic prediction of the rotor in hover and forward flight remains the capturing of the tip vortex or representing its effects adequately. Until recently, this representation was externally input from empirical/analytical models because full Euler/Navier–Stokes (NS) computations were infeasible. With the enormous advances in computational methodologies and computational power, researchers have been adapting Euler/NS techniques for the study of the rotor flowfield. These first-principles-based solvers are particularly useful in analyzing new or complex rotor blades where no experimental data are available. Studies by Srinivasan and Ahmad,[1] Strawn and Barth,[2] Duque and Srinivasan[3] and Duque[4] have used a variety of strategies, such as unstructured methodologies and overset methodologies, to tackle this problem. An excellent survey article by McCroskey[5] gives a comprehensive review of modern computational strategies for rotor applications.

Hariharan and Sankar[6,7] used high-order methods to capture the vortices accurately over long distances and, thus, compute the rotor flowfield with a high-resolution scheme. An alternative method of retaining the vortex fidelity by introducing nondissipative terms has been explored and furthered by Wang, Steinhoff et al.[8] This method, known as vortex confinement, tries to confine a vortex from enlarging due to dissipation by modifying the momentum equations.

One of the central issues facing the future of first-principles based Euler/NS simulation as a practical and useful tool for rotorcraft issues is their ability to capture vorticity without numerical dissipation. Despite the tremendous advances in high-order vortex modeling, none of the methods have yet been demonstrated to be able to capture the vortex with sufficient resolution (less than 10% dissipation) over one revolution of the tip vortex. Such a resolution is necessary to study critical issues such as vortex miss distance and blade/vortex interaction (BVI). Is it possible at all using first-principles Euler/NS simulations to achieve such a realistic objective with reasonably sized grids? What sorts of minimum grid density requirements can one hope to have without diffusing the vortex?

In this effort, we evaluate fifth-/seventh-order spatially accurate methods to answer the preceding questions. Even with the use of such high-order methods, enough grid points have to be provided at locations where vortices occur. An overset grid adaptation/refinement scheme is used in this work to provide high-density grid points only in regions where they are required. Before the high-order methods for rotor wakes are applied, it is instructive to compare the benefits of using these high-order schemes in a wing tip vortex-capturing validation and evaluation. For this purpose, detailed velocity profile comparisons between computed and experimental results for tip vortices off a NACA0015 wing are presented in this paper.

II. High-Order Euler/NS Formulation

The discretized form of three-dimensional unsteady finite volume version of the NS equation is solved:

$$\frac{\partial}{\partial t}(\boldsymbol{q}\Omega_J) + \sum_{i=1}^{6}[(\boldsymbol{V}_F - \boldsymbol{V}_G)\boldsymbol{q} + \boldsymbol{F}]\cdot\Delta S = \sum_{i=1}^{6}\boldsymbol{F}_v\cdot\Delta S \qquad (1)$$

The preceding formulation allows for arbitrary motion of the grids. The temporal discretization is done using a three-point stencil,[6,7] and the solution update process uses a Newton iterative solver to achieve third-order temporal accuracy. The viscous fluxes are computed using central differences. The inviscid fluxes are updated using

Received 12 November 2001; revision received 5 July 2002; accepted for publication 20 July 2002.

*Senior Engineer, Systems Department; harihans@utrc.utc.com.

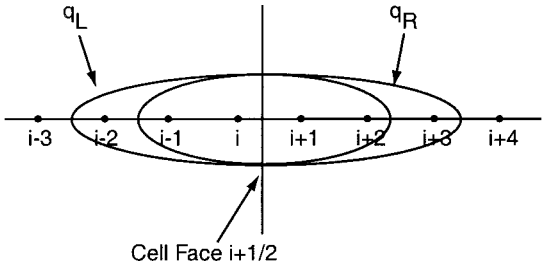

Fig. 1a Fifth-order stencils for computing left and right primitive variables.

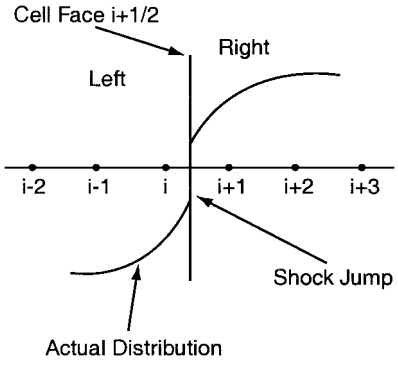

Fig. 1b Distribution with a discontinuity.

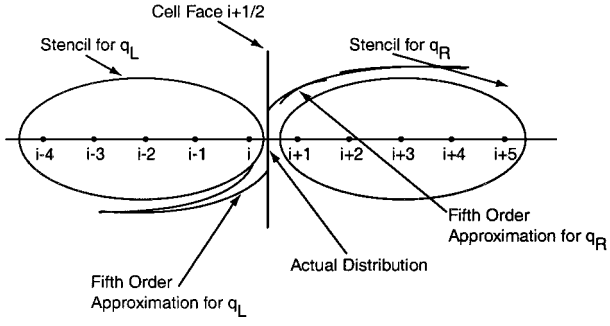

Fig. 1c Adaptive stencil for uniformly high-order solution.

an approximate Riemann solver, that is, the numerical flux on the cell faces is given by

$$\boldsymbol{F} = [\boldsymbol{F}_1(\boldsymbol{q}_L) + \boldsymbol{F}_1(\boldsymbol{q}_R)]/2 - |A|(\boldsymbol{q}_R - \boldsymbol{q}_L) \tag{2}$$

A. Baseline Fifth-Order Essentially Nonoscillatory (ENO) Scheme

The fifth-order formulation in the solver has been developed along the lines of essentially nonoscillatory (ENO) methods by Harten et al.[9] The higher-order reconstruction comes in the projection stage of the conservative variable, that is, $\boldsymbol{q}_L$ and $\boldsymbol{q}_R$. For a smoothly varying function, these projections are based on the support stencils as shown in Fig. 1a.

The details of the economic implementation of this scheme can be found elsewhere, for example, in Refs. 6 and 7. The fifth-order ENO scheme required 10% more computational resources when compared to the widely used third-order spatially accurate MUSCL scheme.[7] In case a discontinuity is present in the sampling region (i.e., as illustrated in Fig. 1b), the sampling stencils are automatically shifted to avoid sampling across the discontinuity, as shown in Fig. 1c. A third-order Newton iterative scheme is used to integrate in time. The time stepping is done in an implicit manner using directional factorization.[7]

B. Seventh-Order Scheme

The seventh-order extension is constructed along similar lines to those just mentioned. A wider stencil, as shown in Fig. 2, is used for the left and right projection. The stencil shifting near the boundaries and discontinuities is similar to the baseline implementation.

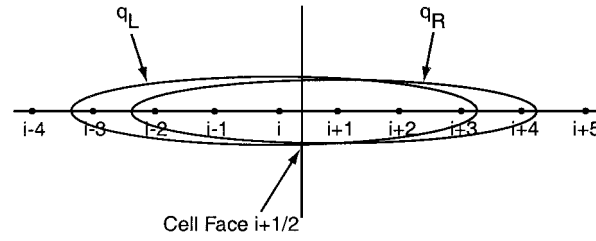

Fig. 2 Seventh-order stencil for smooth flow conditions.

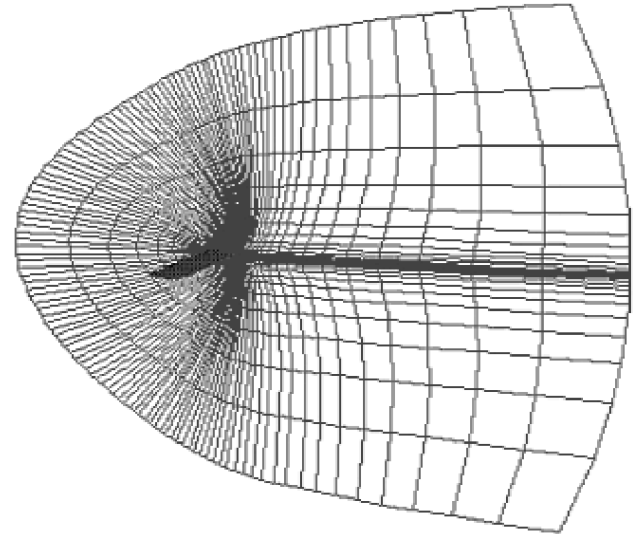

Fig. 3 Spanwise section of the grid for the wing tip vortex study.

C. Three-Dimensional Unsteady Overset Framework

The fifth-/seventh-order ENO formulations were cast in an overset grid solution framework. In an overset framework, different parts of a flow solution problem are gridded independently and placed in space. Information exchange between the solutions being computed on different grids is achieved by trilinear interpolation. This process is usually referred to as grid connectivity. Hariharan and Sankar[10] have extensively validated the three-dimensional unsteady overset flow methodology used in this effort in earlier rotor-airframe/vortex interaction studies. In the current work, the grid connectivity is computed "on-the-fly," that is, at all time steps of the solution computation. Thus, a priori knowledge of the grid motion in the course of a simulation is not required. A set of grid dynamics subroutines updates the position of the grids after each time step. This grid motion could be prescribed, that is, forward motion of the body, as rotary motion of the blade grid, etc. The grid motion could equally well be the distortive grid motion when such grids are used to track features such as tip vortices. Details of implementation of self-adaptive, overset grid tracking of vortices are described in Ref. 11. In the simulations in this effort, both of the components of the grid motion will be involved.

III. Results and Discussions

A. Computation of a Wing Tip Vortex: Fifth-Order ENO vs Third-Order MUSCL

A NACA0015 blunt-edged wing tested by McAllister and Takahashi[12] was chosen for this study because extensive velocity profile measurements are available from this experiment. A C grid consisting of 121 points in the streamwise direction, 25 points in the spanwise direction, and 31 points in the normal direction was constructed. The grid was rapidly stretched in the downstream direction to span over a distance of 15 chord lengths behind the trailing edge. Some degradation in the solution quality at the downstream

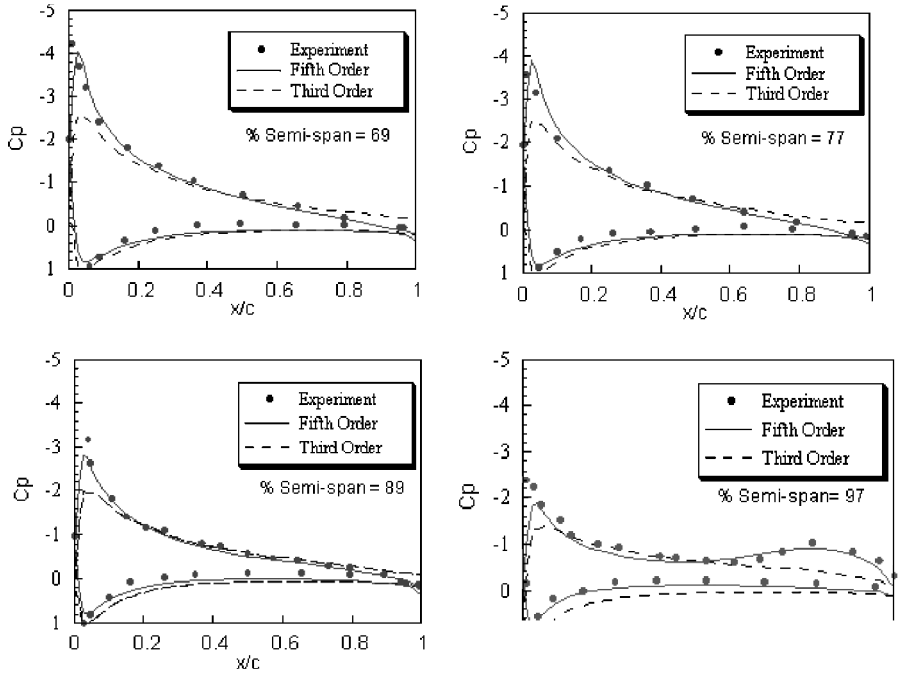

Fig. 4 Surface pressure distribution at various spanwise stations, for a blunt tipped wing.

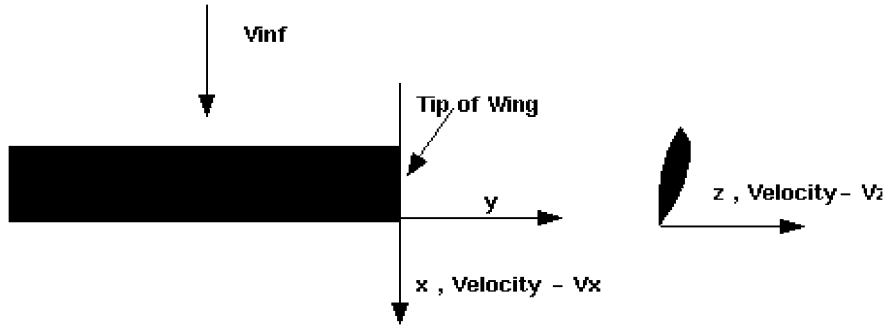

Fig. 5 Schematic of the wing.

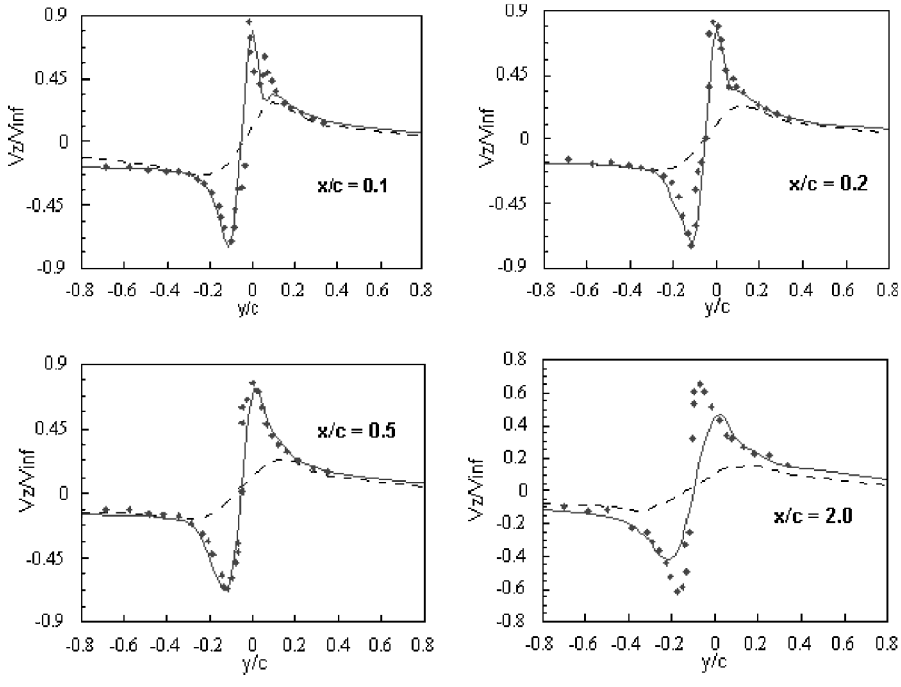

Fig. 6 Downward velocity V_Z distribution across the tip vortex at various downstream locations: – – –, Euler third-order MUSCL; ——, Euler fifth-order ENO; and ♦, experiment.

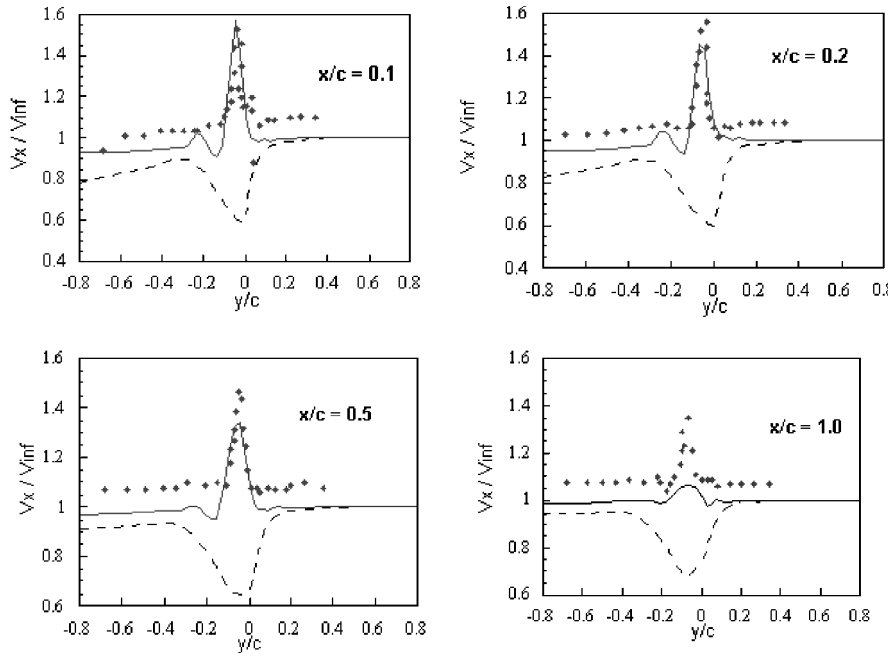

Fig. 7 Axial velocity V_X distribution across the tip vortex at various downstream locations.

locations was then inevitable. Figure 3 shows a spanwise section of the grid.

Figure 4 presents the surface pressure distribution comparison between baseline third-order baseline MUSCL[1,4] scheme and fifth-order ENO scheme at four spanwise stations. The baseline third-order MUSCL is used widely in other first-principles-based Euler/NS computations.[1,4] The solution computed by the fifth-order scheme is found to be superior at all of the stations, comparing better with the experimental values. In the inboard stations (semispan of 69 and 77%), the suction peak is picked up better by the fifth-order scheme, and the overall agreement with experiment is better. Very close to the tip (semispan of 97%), the difference between the third- and the fifth-order scheme is more marked. The fifth-order scheme picks up the rear bump in the suction side caused by the formation of the tip vortex and the subsequent rollover. This is entirely missed by the third-order scheme. A visualization study on the formation of the tip vortex presented later analyzes this issue further.

For the study of tip vortex evolution, these calculations were repeated with 40 points in the spanwise direction, retaining the same number of points in the other two directions. Figure 5 shows a schematic of the system and the coordinate system. Figure 6 shows the downward velocity V_Z profile across the tip vortex at various streamwise locations behind the trailing edge. The fifth-order solution is again found to be superior to the third-order solution. Immediately behind the trailing edge ($x/c = 0.1$, 0.2, and 1.0), the fifth-order solution agrees very well with the experiments. At around $x/c = 2.0$, the velocity peaks captured by the fifth-order scheme start diminishing when compared to experiments. The grid stretching in the streamwise direction becomes too large to produce the exact peak. On the other hand, the third-order solution produces an even weaker and more diffuse vortex.

Figure 7 shows the axial velocity V_X across the tip vortex at various streamwise stations. Predicting the axial velocity field inside a vortex is more difficult because the formation of the axial velocity distribution is a secondary effect. All reasonably accurate schemes can capture V_Z distribution to some extent or other, as was seen earlier. For example, in Fig. 6, even though the third-order solution produced a diffused vortex, it predicted the correct trend in the downward velocity across the vortex. However, the axial velocity V_X distribution depends, among other factors, on how the tip vortex forms. As can be seen in Fig. 7, for the given grid density, the third-order scheme is totally off in predicting the axial velocity field, picking up a wrong trend in the distribution. The fifth-order solution not only picks up the right trend, but also agrees reasonably well with experiments in the vicinity of the trailing edge.

Figure 8 shows a series of snapshots comparing streamwise vorticity contours, from the third- and the fifth-order solutions, at various streamwise stations. In each snapshot, the top of Fig. 8a shows the fifth-order solution, and the bottom of Fig. 8a shows the third-order solution. Each snapshot also shows the maximum and minimum value of the streamwise vorticity for both the solutions. The x/c values at the bottom indicate the streamwise location of that snapshot, with $x/c = 0$ corresponding to the wing trailing edge.

The evolution of the vortex over the wing surface is distinctly different between the two schemes. The fifth-order solution produces a vortex that is more concentrated, and the core of the vortex rolls over inboard of the tip, over the wing surface. As it rolls over, a smaller counter-rotating vortex seems to be produced, sandwiched in between the wing surface and the main vortex. This rollover causes lower pressures near the tip region on the suction side. This was evident in the surface pressure distribution at 97% semispan in Fig. 4. As the vortex leaves the wing, it takes on a circular shape, which is seen to be maintained in the downstream region. In contrast, the vortex produced by the third-order solution remains aligned with the grid near the wing tip region as the vortex evolves over the wing tip. This vortex becomes diffused and distorted. This is also evident if the maximum vorticity at any given station is compared between the two solutions.

B. Overset Capturing of Tip Vortex: Fifth-Order ENO Scheme

For a C-type grid topology and for the given number of grid points, even with the use of the fifth-order scheme, the vortex peak-to-peak velocity drops off after around two chord lengths. Enough grid points have to be provided to capture the vortex for much larger distances. To achieve an efficient distribution of grid points, an overset grid strategy is adopted. A wing grid-vortex grid overset system, as shown in Fig. 9, is considered here. The vortex grid extends up to 18 chord lengths behind the wing trailing edge. In this computation, a NACA0015 wing at $\alpha = 15$ deg and $M_\infty = 0.18$ was used again. The existing fifth-order spatial ENO/third-order temporal implicit scheme was used for this study. The purpose of this study is

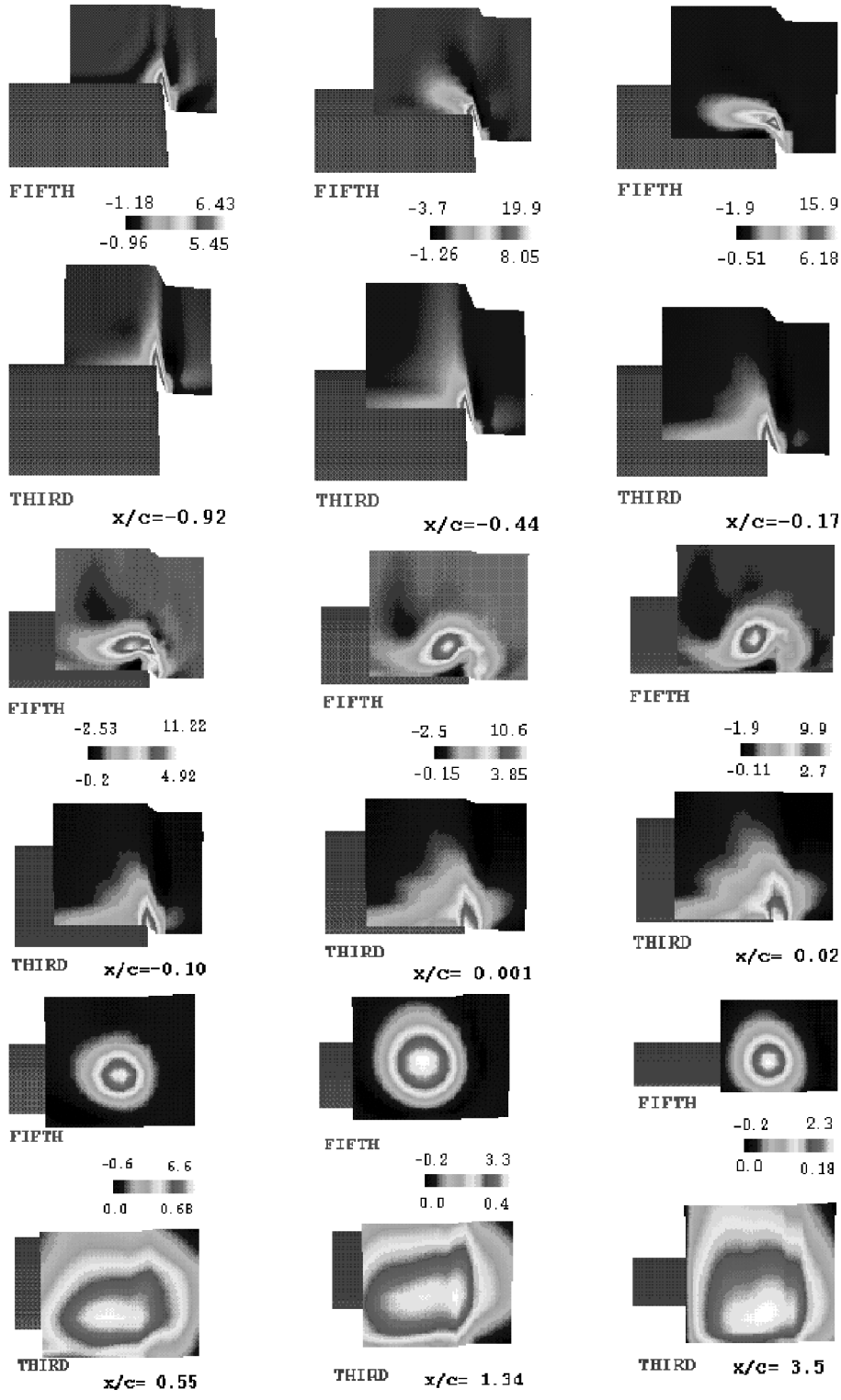

Fig. 8 Comparison of the tip vortex evolution between the fifth- and the third-order schemes. Streamwise vorticity contour plots.

to demonstrate the feasibility of using body-fitted wing/rotor grids with self-deforming vortex grid systems to capture vortices fully over long distances without diffusion, that is, capture the tip vortex over 180 deg of revolution with less than 5–10% dissipation of the peak-to-peak variation of the tip vortex. For a model rotor blade of aspect ratio $AR = 6$, a 180-deg convection would entail $\sim 18\,(\pi \times AR)$ chord lengths of vortex transport, which is the same length as the one considered here. The vortex is generated by the wing grid and transferred to the vortex grid. The vortex grid used for this study had 100 streamwise points and 30×30 points at every streamwise station.

Figures 10 show a view of the initial vortex grid and the self-adapted vortex grid after the computation had converged. Figure 11 shows the axial momentum component on a cross section of the vortex. It is instructive to compare the axial velocity/momentum component because it has a much steeper gradient and is, hence, more difficult to capture without numerical diffusion for a given grid. The captured vortex has a positive axial momentum (jetlike) until around the halfway mark of the 18 chords. Then, it switches over to a negative axial momentum, exhibiting a wake-like behavior. A real physical vortex exhibits a similar behavior due to viscosity.

However, the current simulation is inviscid, and such a transition is incorrectly triggered by the dissipation in the numerics. The axial velocity component in a realistic vortex (over a wing or a rotor) plays an important role in the determination of the vortex structure. A closer look at the variation of the axial and tangential velocity components reveals the need for accurately capturing the axial velocity. Figures 12a–12d show the axial and tangential momentum components across the vortex at several streamwise stations.

The fifth-order Euler simulation capturing the vortex (Figs. 12a–12d) exhibits the following behavior. If the axial velocity is correctly represented, that is, jetlike, then the peak-to-peak tangential velocity variation remains at a certain value. If the axial velocity dissipates (due to numerical dissipation) below zero, it switches to a wakelike structure, changing the peak-to-peak tangential velocity variation to a different lower value. In the current study, the axial velocity component switches mode at around the 40% mark of the required length of the vortex grid. Thus, to capture the right value of the peak-to-peak tangential variation, it is necessary to capture the correct axial mode (jetlike vs wakelike). Even if the axial velocity component does not play a big role in a certain physical interaction, that is, certain BVI, for the purpose of correctly capturing the tangential peak-to-peak variation, the axial velocity component has to be captured correctly. The axial component has much steeper gradients, and, hence, it dissipates faster. The vortex grid used in the current study had 30×30 points in the cutting plane across the vortex. This may have to be enhanced to two or three times this size to capture the vortex without any dissipation using the baseline fifth-order ENO scheme. Alternatively, we can increase the spatial accuracy further and capture the vortex with the current or even smaller grids. We analyze the performance of a seventh-order scheme in the next study.

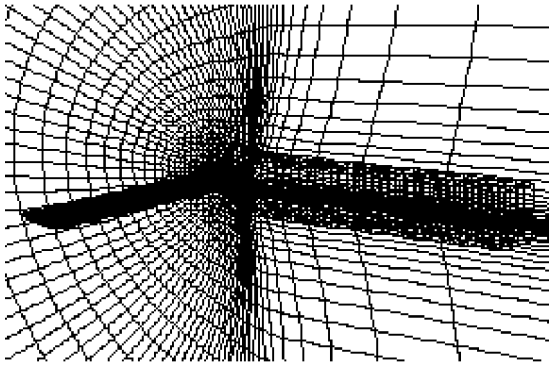

Fig. 9 Wing grid-vortex grid overset system.

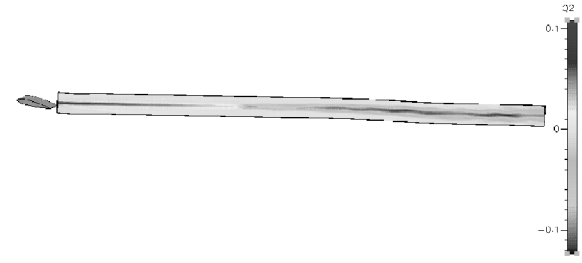

Fig. 11 Streamwise momentum contours across spanwise section of the vortex grid.

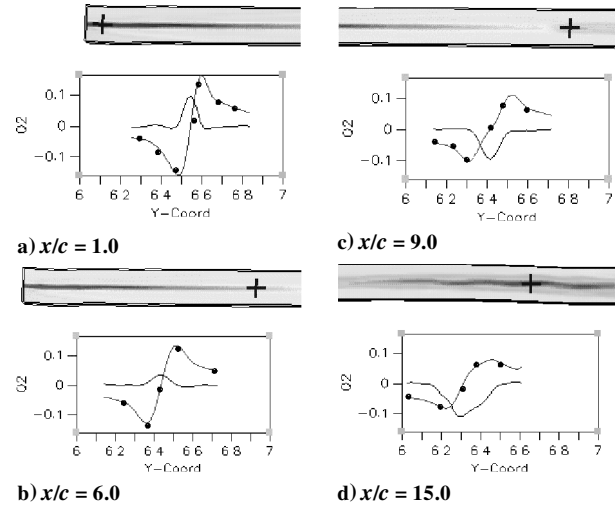

Fig. 12 Comparison of axial and tangential momentum variation across the vortex: ——, axial momentum and ● ● ●, tangential momentum.

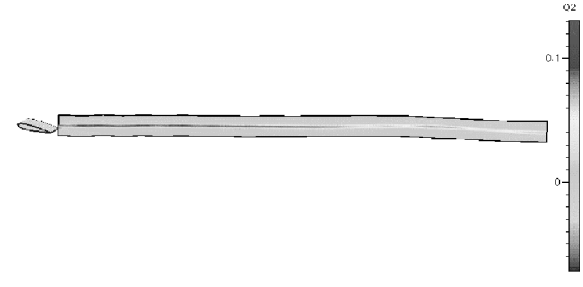

Fig. 13 Axial momentum contours across a spanwise section of the vortex grid.

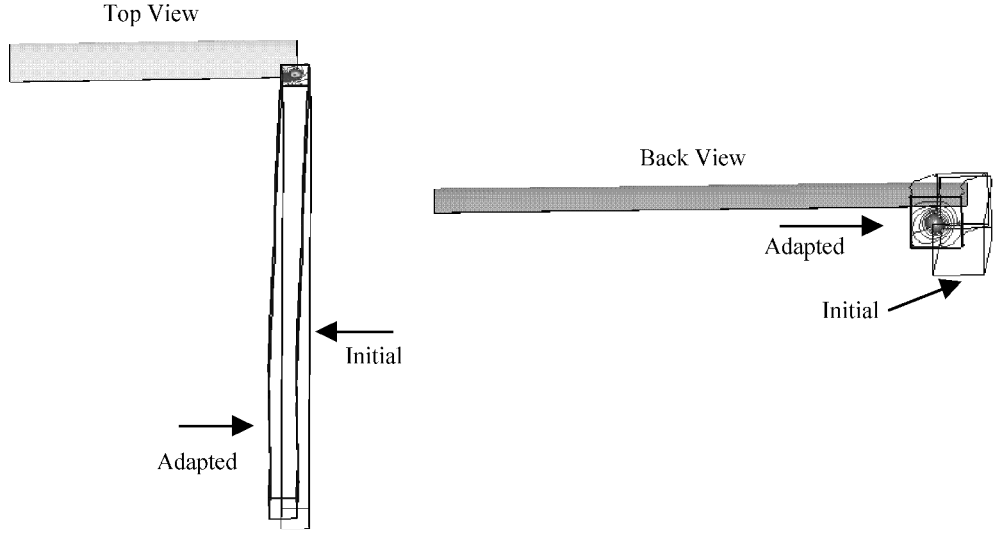

Fig. 10 Initial and adapted vortex grid.

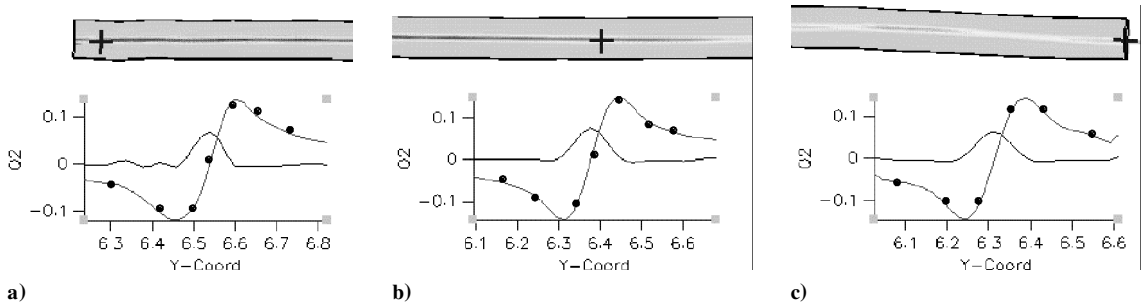

Fig. 14 Axial and tangential momentum variation across the vortex at various streamwise sections.

Table 1 Comparison of run time[a]

Scheme	CPU time/iteration, s
Fifth ENO	13.5
Seventh ENO	17.2

[a]Overset system: grid 1 consists of $90 \times 40 \times 30$ grid points, grid 2 consists of $100 \times 30 \times 30$ grid points, and one iteration is equal to three subiterations. The simulations were run in a DEC alpha 500 workstation.

C. Overset Capturing of Tip Vortex: Seventh-Order ENO Scheme

The analysis of wing vortex convection using fifth-order ENO gave definite pointers toward capturing rotor tip vortices accurately without an excessive number of grid points. With around eight points across the vortex core, the fifth-order scheme captures the tangential velocity variation, but the axial velocity tends to get dissipated when the convection distances are more than 10 chord lengths. The question arises of whether increasing the order of accuracy further will be more effective.

Of direct interest are the three queries as to 1) stability, 2) increased cost of computation per iteration, and 3) payoffs in terms of the ability to resolve the vortex. The same grid system as in the study in Sec. III.B was considered. To keep the comparisons fair and simple, the vortex itself is generated using the baseline fifth-order scheme and transferred to the vortex grid. The seventh-order scheme is applied to the vortex grid alone. The computation inside the vortex grid is uniformly seventh-order accurate, using one-sided stencil shift near the boundaries.

The stability was not affected, given that the vortex grid is fairly simple. The same time stepping that was applied using the fifth-order computation was retained for the seventh-order scheme. The timing comparison between the two schemes is shown in Table 1.

The seventh-order scheme costs 27% more in terms of computational expense when compared to the fifth-order scheme.

Figure 13 shows the axial momentum contour across a spanwise plane cutting the vortex. The axial momentum variation is captured with very little dissipation over the entire ~18 chord lengths. The axial momentum contours appear diminished in patches toward the 70 and 90% marks. This is because the vortex "wiggles" sideways, and the maximum does not always stay in the same plane. Figures 14a–14c compare the axial and tangential velocity variation at the 5, 50, and 100% marks of the length of the vortex grid, respectively. The axial component has very little dissipation, and the tangential component has no noticeable dissipation. The seventh-order scheme requires around five points across the vortex face to capture both the axial and tangential velocity accurately.

The seventh-order solution vastly outperforms the fifth-order solution for the extra effort involved. With the given grid, the fifth-order convects up to a distance of ~7 chord lengths before axial momentum variation flips. The seventh-order solution has captured up to ~18 chord lengths with little dissipation and could potentially capture ~40–50 chord lengths (or, in terms of the rotor, ~3–4 half-revolutions for a model rotor of $AR = 6$) with the given grid density.

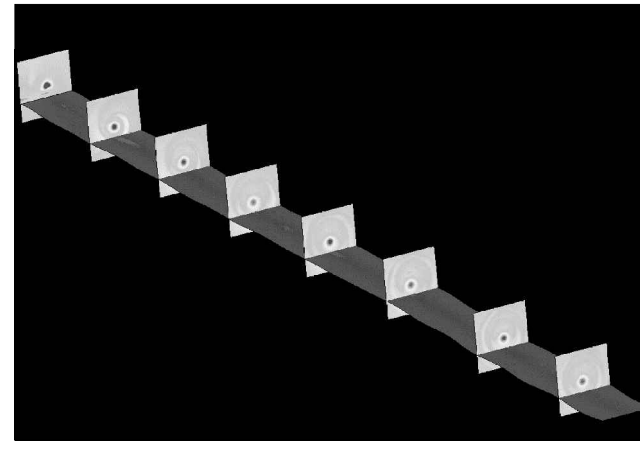

Fig. 15 Axial momentum contours at several streamwise stations.

Figure 15 shows the axial momentum contours at several streamwise stations. Even the vortex sheet rollup is captured and can be seen 18 chord lengths away.

The next challenge is to extend this methodology for the application to a realistic rotor blade such as the UH60 and compare the results with experiments and similar lower-order first-principles predictions by Strawn and Ahmad.[13]

IV. Conclusions

Fifth-/seventh-order spatially accurate ENO schemes have been applied in conjunction with overset vortex refinement to capture tip vortex off of a blunt wing tip. The following conclusions can be made from this study:

1) To capture the vortex with few points, one can, in principle, keep increasing the order of computation. However, the effect of a much larger stencil on stability, intergrid information degradation, and effects of lower-order-grid metrics eventually offset the advantages of using high-order schemes beyond a point. The seventh-order scheme was found to work well when used with Cartesian grids where grid metrics computation is trivial. The seventh-order computation resolves the tip vortex using approximately five points across the vortex.

2) Overset vortex grid refinement can be employed to reduce the grid point requirements. This methodology will have its own challenges when applied for a system with many vortices. It is not easy to maintain grid smoothness when deforming the vortex grid to track a complicated vortex system.

References

[1]Srinivasan, G. R., and Ahmad, J. U., "Navier–Stokes Simulation of Rotor-Body Flowfield in Hover Using Overset Grids," Paper C15, 19th European Rotorcraft Forum, Confederation of European Aerospace Societies, Sept. 1993.

[2]Strawn, R. C., and Barth, T. J., "Unstructured Adaptive Mesh Computations of Rotorcraft High-Speed Impulsive Noise," *Journal of Aircraft*, Vol. 32, No. 4, 1996.

[3]Duque, E. P. N., and Srinivasan, G. R., "Numerical Simulation of a Hovering Rotor Using Embedded Grids," American Helicopter Society, 48th Annual AHS Forum, May 1992.

[4]Duque, E. P., "A Structured/Unstructured Embedded Grid Solver for Helicopter Rotor Flows," American Helicopter Society, 50th Annual AHS Forum, May 1994.

[5]McCroskey, W. J., "Wake Vortex System of Helicopters," AIAA Paper 95-0530, Jan. 1995.

[6]Hariharan, N., and Sankar, L.N., "Higher Order Numerical Simulation of Rotor Flow Field," American Helicopter Society, Forum and Technology Display, May 1994.

[7]Hariharan, N., and Sankar, L. N., "Application of ENO Schemes to Rotary Wing Problems," AIAA Paper 95-1892, June 1995.

[8]Wang, C. M., Steinhoff, J. S., and Stremel P. M., "A New Numerical Approach for Rotor Craft Aerodynamics Using Vorticity Cofinement," AIAA 97-2328, AIAA Applied Aerodynamics Conf., Atlanta, GA, June 1997.

[9]Harten, A., Engquist, B., Osher, S., and Chakravarthy, S. R., "Uniformly High Order Accurate Essentially Non-Oscillatory Schemes III," *Journal of Computational Physics*, Vol. 131, No. 1, Feb. 199**X**, pp. 3, 4.

[10]Hariharan, N., and Sankar, L.N., "Numerical Simulation of Rotor–Airframe Interaction," AIAA Paper 95-0194, 33rd AIAA Aerospace Sciences Meeting, Jan. 1995.

[11]Hariharan, N., "A High Order Overset Refinement Methodology for Vortex-Dominated Flowfield Studies," AIAA Paper 2002-0965, Jan. 2002.

[12]McAlister, H. W., and Takahashi, R. K., "NACA0015 Wing Pressure and Trailing Vortex Measurements," U.S. Army Aviation Systems Command, NASA TP 3151, NASA Ames Research Center, CA, TR-91-A-003, 1991.

[13]Strawn, R. C., and Ahmad, J. U., "Computational Modeling of Hovering Rotors and Wakes," AIAA Paper 2000-0110, Jan. 2000.